

HCS-TNAS: Hybrid Constraint-driven Semi-supervised Transformer-NAS for Ultrasound Image Segmentation

Renqi Chen^{1,2}, Xinzhe Zheng³, Haoyang Su^{2*}, Kehan Wu⁴

¹Fudan University, Shanghai, China

²Shanghai Artificial Intelligence Laboratory, Shanghai, China

³The University of Hong Kong, Hong Kong, China

⁴Southern University of Science and Technology, Shenzhen, China

{chenrenqi, suhaoyang}@pjlab.org.cn, zxz.krypton@outlook.com, 12010519@mail.sustech.edu.cn

Abstract

Precise ultrasound segmentation is vital for clinicians to provide comprehensive diagnoses. However, developing a model that accurately segments ultrasound images is challenging due to the images' low quality and the scarcity of extensive labeled data. This results in two main solutions: (1) optimizing multi-scale feature representations, and (2) increasing resistance to data dependency. The first approach necessitates an advanced network architecture, but a handcrafted network is knowledge-intensive and often yields limited improvement. In contrast, neural architecture search (NAS) can more easily attain optimal performance, albeit with significant computational costs. Regarding the second issue, semi-supervised learning (SSL) is an established method, but combining it with complex NAS faces the risk of overfitting to a few labeled samples without extra constraints. Therefore, we introduce a hybrid constraint-driven semi-supervised Transformer-NAS (HCS-TNAS), balancing both solutions for segmentation. HCS-TNAS includes an Efficient NAS-ViT module for multi-scale token search before ViT's attention calculation, effectively capturing contextual and local information with lower computational costs, and a hybrid SSL framework that adds network independence and contrastive learning to the optimization for solving data dependency. By further developing a stage-wise optimization strategy, a rational network structure is identified. Experiments on public datasets show that HCS-TNAS achieves state-of-the-art performance, pushing the limit of ultrasound segmentation.

1 Introduction

Ultrasound is a critical medical imaging tool for diagnosing cardiac diseases, where precise segmentation of ultrasound images can further assist clinicians in comprehensively analyzing cardiac conditions (Leclerc et al. 2019). Nevertheless, the development of robust and efficient segmentation algorithms is challenged by issues such as the scarcity of annotated data, speckle noise in ultrasound images, and the difficulty in distinguishing adjacent anatomical structures (Zhou et al. 2023), which necessitates (1) **optimizing multi-scale feature representation**, and (2) **enhancing resistance to data dependency**.

In recent years, deep learning for medical image segmentation has witnessed a progression in understanding multi-scale features. Ronneberger et al. (2015) proposed the U-

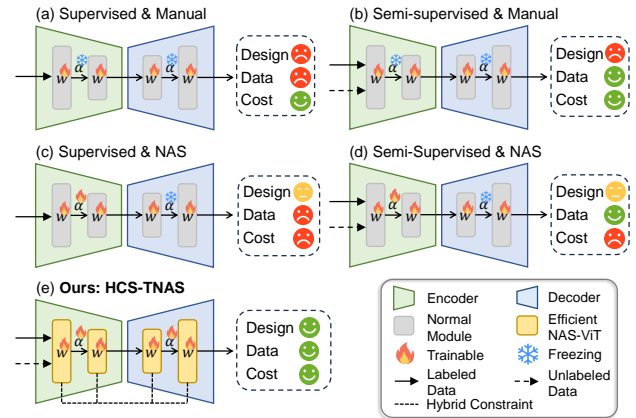


Figure 1: An illustration comparing HCS-TNAS with existing baselines for segmentation task. We use smiley, neutral, and sad faces to present the performance. “Design” denotes the optimization of model architecture, “Data” denotes the resistance to data dependency, and “Cost” denotes the computational resource consumption. α and w present architecture and weights, respectively.

Net, which exhibited extraordinary feature extraction ability, and then the U-shaped encoder-decoder network garnered attention and spawned multiple variants, such as UNet++ (Zhou et al. 2019). While these works focused on local feature perception, the vision Transformer (ViT) (Dosovitskiy et al. 2020) was proposed with a context-sensing ability to capture the relationship between distant pixels. Subsequently, Chen et al. (2021a) proposed TransUNet, which combined a U-shaped network with ViTs, balancing both local and global features. Cai et al. (2023) proposed EfficientViT, which employs multi-scale linear attention to efficiently enhance the multi-scale feature representation.

However, handcrafted networks require substantial expertise to design a rational structure for optimizing multi-scale feature representation. Conversely, Neural Architecture Search (NAS) has gained popularity for its ability to optimize the network structures within a coarse search space, potentially resolving this issue by achieving the optimal structure. Following the introduction of a hierarchical NAS known as Auto-DeepLab (Liu et al. 2019), which garnered

*Corresponding author.

significant attention in the general domain, NAS has been adapted for ultrasound image segmentation, exemplified by SSHNN (Chen et al. 2024). Nevertheless, contemporary NAS approaches in ultrasound image segmentation often indiscriminately increase the search space without considering efficiency, leading to substantial parameter burdens with only marginal enhancements. This issue is primarily due to the vanilla multi-scale feature understanding stemming from constrained representational capacity, an aspect we aim to address in our research.

On the other hand, ultrasound medical image datasets often suffer from a scarcity of labeled data, which hinders the performance of traditional supervised models. Therefore, leveraging unlabeled data for segmentation tasks becomes crucial, and semi-supervised learning (SSL) offers an effective approach. Current SSL methods, such as mean teacher (Tarvainen and Valpola 2017) and co-training (Chen et al. 2021b), efficiently enhance model robustness against data dependency and have been employed for segmentation tasks. Consequently, the integration of NAS with SSL presents a promising avenue for addressing the two challenges inherent in ultrasound image segmentation.

Se²NAS (Pauletto et al. 2022) pioneered the concept of NAS-SSL integration for segmentation tasks, resulting in enhanced performance. Nonetheless, prior research has only executed a basic combination of NAS and SSL, without considering extra constraints during NAS training. This leads to overfitting towards limited labeled data, especially when the structure of NAS is complex. Inspired by CauSSL (Miao et al. 2023), which additionally considers algorithmic independence through co-training to achieve remarkable outcomes, we develop a hybrid constraint-driven SSL framework, leveraging the structural characteristics of NAS to design constraints for training.

To address the aforementioned issues, we propose HCS-TNAS, a hybrid constraint-driven semi-supervised Transformer-NAS for ultrasound image segmentation. We outline the distinctions between our method and seminal methods in Fig. 1. To optimize multi-scale feature representation, we implement hierarchical NAS for feature searching at multiple levels. At the basic cellular level, we propose an Efficient NAS-ViT module that combines NAS with ViT for multi-scale token optimization while reducing computational costs; at the higher module level, NAS is tailored within the encoder and decoder, each with designated search spaces to maintain their distinct functionalities. For the issue of data dependency, we consider multiple constraints on top of the co-training to overcome the overfitting as SSL is employed on complex NAS training. This includes (1) calculating network independence loss with a NAS-based optimization strategy, which promotes algorithmic independence and complementary between two models, fostering diverse representations, and (2) calculating contrastive loss based on the hierarchical architecture, which assists in maximizing mutual information across different views to enhance feature representation and promote generalization capability.

In summary, the main contributions of this paper are:

(1) We propose a Hybrid Constraint-driven Semi-supervised Transformer-NAS for ultrasound image segmen-

tion, addressing two main issues: optimizing multi-scale feature representation and minimizing data dependency.

(2) We adopt NAS for the issue of multi-scale feature representation optimization. Specifically, we design an Efficient NAS-ViT module to generate multi-scale tokens. To the best of our knowledge, this is the first study that introduces NAS into the ViT for token-level searching.

(3) We propose a hybrid constraint-driven SSL for the issue of data dependency. Building upon the co-training, we incorporate algorithmic independence and contrastive learning as additional constraints into a multi-stage optimization strategy to tackle the overfitting under limited annotations.

(4) Extensive experiments on three public ultrasound image datasets demonstrate the advancement of HCS-TNAS.

2 Related Work

2.1 Neural Architecture Search

NAS is proposed to address the difficulty of network design and find the optimal network architecture within the search space. After the introduction of differentiable architecture search (DARTS) (Liu et al. 2018), which created a continuous relaxation algorithm to provide differentiable candidate operation weights, gradient-based NAS became efficiently trainable. Then, PC-DARTS (Xu et al. 2019) proposed partial channel connections and edge normalization, further reducing GPU memory consumption. Edge normalization also inspired the hierarchical NAS (HNAS), enabling a multi-level search. Liu et al. (2019) proposed Auto-DeepLab, which optimizes the network at cell and layer levels. Moreover, the Transformer is used in HNAS to compensate for the lack of context information. In HCT-Net (Yu, Lee, and Chen 2023), Yu et al. utilized a Transformer to process feature maps of varying resolutions. Yang et al. (2023) proposed DAST which incorporates the Transformer layer as candidate operations for cell-level searching. In contrast to them, we search architecture in a larger search space. To reduce parameter costs and search for better multi-scale feature representation, we implement a novel NAS-ViT module.

2.2 SSL for Medical Image Segmentation

SSL can alleviate the scarcity of labeled data in medical image segmentation, which can be categorized into pseudo-labeling methods and consistency regularization methods. The former produces pseudo-labels for unlabeled data in training, such as self-training (Bai et al. 2017). Moreover, Wang et al. (2021) adopted uncertainty-guided confidence-aware refinement to mitigate the influence of low-quality pseudo-labels. For consistency regularization methods, Tarvainen et al. (2017) proposed mean teacher (MT), which averaged weight parameters to form a teacher model for promoting consistency between predictions and targets. Then, Yu et al. (2019) proposed an uncertainty-aware MT which enables the student to learn from reliable targets. Apart from the MT framework, Qiao et al. (2018) achieved a Deep co-training framework, learning two networks on two views to provide complementary information. Xia et al. (2020) developed the uncertainty-aware multi-view co-training (UMCT),

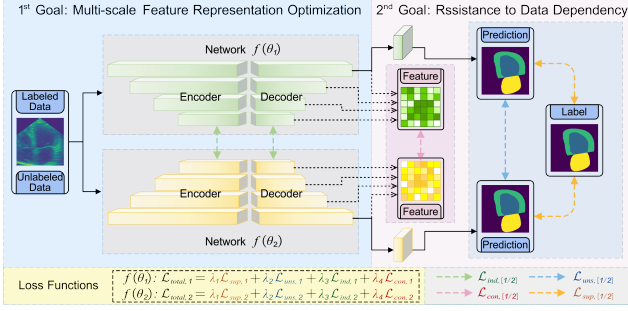


Figure 2: The pipeline of HCS-TNAS. The hierarchical structure of NAS networks serves for the goal of multi-scale feature representation optimization and multi-constraint SSL serves for the goal of resistance to data dependency.

proving the effectiveness of multi-view consistency in co-training. In this work, we opt to design a hybrid constraint-driven SSL framework, considering network constraints from the perspective of NAS architecture.

3 Methodology

An overview of the proposed HCS-TNAS is shown in Fig. 2. For the first goal, our framework uses two networks: $f(\theta_1)$ and $f(\theta_2)$, where both networks share the same hierarchical NAS backbone (Sec. 3.2) but use different parameters and independent optimizers. Specifically, to integrate NAS with ViT for multi-scale feature representation optimization and address the resource-intensive issue of NAS, we propose an Efficient NAS-ViT module (Sec. 3.1) in the NAS backbone.

For the second goal, we adopt a hybrid constraint-driven SSL framework (Sec. 3.3) and corresponding stage-wise optimization strategy (Sec. 3.4) to update network parameters and enhance the resistance to data dependency, consisting of two manifold constraints upon the co-training scheme.

3.1 Efficient NAS-ViT Module

In DAST (Yang et al. 2023), the ViT layer is treated as the candidate operation for multi-scale feature representation, leading to increased computation complexity. On the other hand, since the ViT is more complex than other operations, the model tends to select the ViT during backbone optimization, rendering the search meaningless. To solve these, we use the ViT as the basic unit, further implementing NAS before the attention calculation for searching multi-scale tokens, termed Efficient NAS-ViT. Compared to EfficientViT, where tokens are processed by fixed multi-scale convolution and sent into attention separately, our design can obtain a better multi-scale feature representation while reducing excessive parameter overhead. The effectiveness of this novel Transformer-based approach for NAS is proven through the empirical results (Sec. 4.4). An overview of the Efficient NAS-ViT is shown in the “Efficient NAS-ViT” of Fig. 3(c), used in the encoder NAS’s inner cell search.

Given input x after linear projection, tokens $Q = xW_Q$, $K = xW_K$, $V = xW_V$, where $W_Q/W_K/W_V$ is the learnable linear projection matrix. Rather than using fixed oper-

ations to obtain multi-scale tokens, which constrains the token representation and affects attention calculation, we employ NAS to search for token representations, thereby enhancing the multi-scale learning capability. After incorporating partial channel connections to reduce memory overhead and reusing continuous relaxation for a differentiable search space, the multi-scale tokens $Q'/K'/V'$ are:

$$\{Q'/K'/V'\} = (1 - \mathbf{P}) \odot \{Q/K/V\} + \sum_{O_i \in \mathcal{O}^{en}} \frac{\exp\{\alpha_i\}}{\sum_{j=1}^{|\mathcal{O}^{en}|} \exp\{\alpha_j\}} \cdot O_i(\mathbf{P} \odot \{Q/K/V\}), \quad (1)$$

where \mathbf{P} is the sampling mask for channel selection, \odot denotes Hadamard product, O_i denotes the i -th operation selected from the set of encoder candidate operations \mathcal{O}^{en} (where encoder and decoder consider different sets of candidate operations due to their respective roles, please refer to Appendix A), and α is cell architecture parameter, which measures the weight of related candidate operation. Subsequently, tokens are computed by ReLU linear attention for contextual information:

$$R_n = \sum_{i=1}^S \frac{\text{ReLU}(Q'_n) \text{ReLU}(K'_i)^T}{\sum_{j=1}^S \text{ReLU}(Q'_n) \text{ReLU}(K'_j)^T} V'_i \quad (2)$$

where subscript n denotes the n -th row of R/Q , and S is the sequence length. Then, the output R is fed into the FFN+DWConv layer (which is the application of depthwise convolution on the FFN layer) for local information capture.

3.2 NAS Backbone

Encoder NAS. We have cell- and layer-level searches for the multi-scale feature extraction. There are N intermediate nodes in cell search space, where the edge between nodes corresponds to the proposed Efficient NAS-ViT module, shown in the “Cell-level Search” of Fig. 3(c). After processing inputs by Efficient NAS-ViT ($f_{NAS-ViT}$), the output of the n -th node of the encoder cell in the l -th layer is:

$${}^r H_n^l = \sum_{{}^r H_i^l \in \mathcal{I}} f_{NAS-ViT}({}^r H_i^l; \alpha), \quad (3)$$

where the input set \mathcal{I} includes the previous cell’s output and previous nodes’ outputs in the current cell, and r denotes resolution. To capture multi-resolution features, our model considers six values: $r = 1, 2, 4, 8, 16, 32$, where $r = 1$ corresponds to the original image size. Two stem cells down-sample the input from $r = 1$ to $r = 4$. When $r = 4$, the spatial size of the feature maps is $1/4$ of the case where $r = 1$.

The final output tensor of the cell is the concatenation of outputs from all nodes. For simplicity, the cell-level search is written as $Cell({}^r H^{l-1}, {}^r H^{l-2}; \alpha)$.

The layer-level search aims at aggregating features from different resolutions by employing convolution kernels and skip connections, shown in the “Layer-level Search” of Fig. 3(c). The parameters of these kernels are referred to as the architecture parameters β . There are L layers in the back-

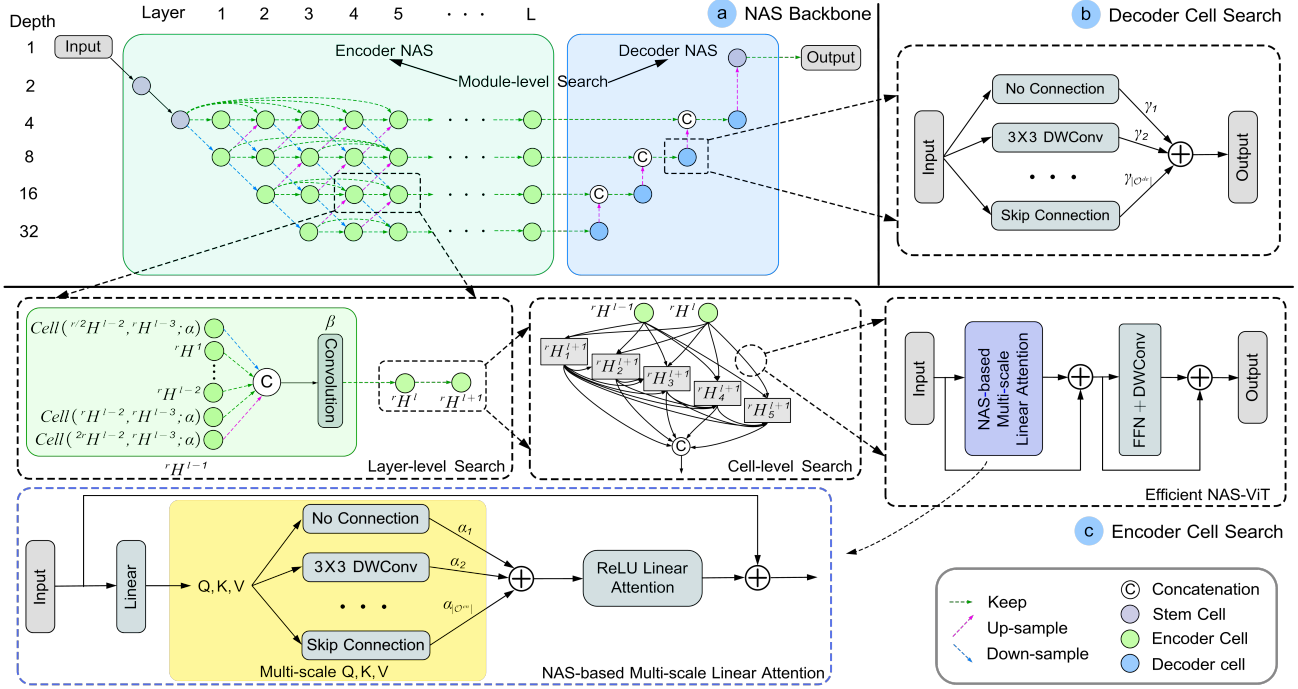


Figure 3: The proposed NAS backbone. (a) shows an overview of the NAS backbone, which consists of an encoder NAS and a decoder NAS, representing a module-level search. The input is passed through the encoder NAS to obtain multi-resolution feature maps, where a hierarchical encoder cell search is performed (shown in (c)). These outcomes are then processed by the decoder cells (shown in (b)), which concatenate features and complete the recovery process through further searching.

bone and the formulation of the l -th layer level search is:

$$\begin{aligned}
 {}^r H^l = & \text{Conv}(\text{Concat}[\text{Down}(\text{Cell}(\frac{r}{2} H^{l-1}, {}^r H^{l-2}; \alpha)), \\
 & \text{Up}(\text{Cell}({}^{2r} H^{l-1}, {}^r H^{l-2}; \alpha)), \text{Cell}({}^r H^{l-1}, {}^r H^{l-2}; \alpha), \\
 & \{ {}^r H^{l'} \in {}^r H | l' < l \}], \\
 & \beta)
 \end{aligned} \quad (4)$$

where $\text{Conv}(\cdot)$ denotes the convolution, transforming fused features to the same channel counts of r -resolution. $\text{Down}(\cdot)$ and $\text{Up}(\cdot)$ denote down- and up-sampling.

Decoder NAS. Rather than employing fixed convolution kernel sizes, we also introduce NAS for the decoder to enhance the capability. A U-shaped architecture is used as the backbone for the decoder NAS, as depicted in Fig. 3(a).

In the decoder NAS, the features from the $r = 32$ layer after the encoder NAS are fed into the decoder cell as the initial input. To mitigate the excessive computational complexity introduced by NAS, the decoder cell does not contain intermediate nodes, as shown in Fig. 3(b). The search is:

$${}^r H^{de} = \sum_{O_i \in \mathcal{O}^{de}} \frac{\exp\{\gamma_i\}}{\sum_{j=1}^{|\mathcal{O}^{de}|} \exp\{\gamma_j\}} \cdot O_i({}^r H^{l=L}), \quad (5)$$

where γ are decoder architecture parameters, and ${}^r H^{de}$ is the final output tensor of decoder cell in r -resolution.

After upsampling, the features ${}^r H^{de}$ are concatenated with ${}^{r/2} H^L$, and a convolution layer is applied to match the number of channels with the $r/2$ decoder NAS. This process

is then repeated until the $r = 4$ features are combined. Finally, an upsample layer is employed to recover the outputs to the full resolution, followed by a convolution layer to obtain the desired number of classes for segmentation tasks.

3.3 Hybrid Constraints-driven SSL

To leverage the unlabeled data, the co-training framework of SSL is implemented, where the unsupervised loss is:

$$\mathcal{L}_{uns,a} = CE(p_{u,a}, \hat{y}_{u,b}) \quad (6)$$

where $a, b \in \{1, 2\}$ and $a \neq b$, corresponds to $f(\theta_a)$ and $f(\theta_b)$, respectively. $CE(\cdot)$ indicates the cross-entropy loss. $p_{u,a}$ is the predicted probability map generated by one network on the unlabeled data, and $\hat{y}_{u,b}$ is the corresponding one-hot pseudo label generated by another.

As the algorithmic independence could facilitate the creation of distinct networks (Miao et al. 2023), especially in the co-training, complementary networks are capable of capturing diverse feature information and are less likely to overfit to a particular subset. Thus, we incorporate network independence loss and propose a stage-wise optimization strategy (See Sec. 3.4) to fully utilize very few samples. The network dependence loss is defined between two NAS backbones based on convolutional layers at the same position:

$$\mathcal{L}_{ind,a} = \frac{1}{L_{CNN}} \sum_{i=1}^{L_{CNN}} IND(\theta_{a,i}, \theta_{b,i}; G_{b,i}) \quad (7)$$

where L_{CNN} is the number of convolutional layers. $\theta_{a,i} \in \mathbb{R}^{C_{out} \times d}$ ($d = K \times K \times C_{in}$) are the weights of the i -th convolutional layer in $f(\theta_a)$, reshaped into a matrix form, where K is kernel size. C_{in}, C_{out} are the number of input and output feature channels. $G_{b,i} \in \mathbb{R}^{C_{out} \times C_{out}}$ is corresponding optimal coefficient matrix. Given matrices A, B, G_B , dependence loss function is:

$$IND(A, B; G_B) = \frac{1}{C_{out}} \sum_{i=1}^{C_{out}} \left(\frac{\mathbf{v}_{A,i} \cdot \mathbf{q}_{B,i}}{|\mathbf{v}_{A,i}| \times |\mathbf{q}_{B,i}|} \right)^2, \quad (8)$$

where $\mathbf{v}_{A,i}$ is the i -th row of A and $\mathbf{q}_{B,i} = (G_B \times B)_i$.

Since algorithmic independence essentially endows the network with the capability to observe the same image from different perspectives, we consider that contrastive loss can be utilized to maximize the mutual information across these views to enhance discriminative feature representation, which also helps the model to generalize to new samples. Benefiting from network independence, there is also no need to construct an asymmetric architecture for contrastive loss.

In this work, an uncertainty-based contrastive loss is calculated based on the hierarchical architecture of NAS, measured on the outputs at different stages of the decoder cell between two networks. The uncertainty estimation is defined using smoothed KL-divergence and considers features at various resolutions:

$$U_a^{r,h,w} = \sum_{c=0}^{C-1} ({}^r_a H^{de})^{c,h,w} \cdot \log \frac{({}^r_a H^{de})^{c,h,w} + \epsilon}{(\overline{{}^r_a H^{de}})^c + \epsilon} \quad (9)$$

where C is the channel dimension, ϵ is a small bias term, $r \in \{4, 8, 16, 32\}$ are used, ${}^r_a H^{de}$ is the output tensor of the decoder cell at the r -resolution. $\overline{(\cdot)}$ is the mean value across the channel dimension. A higher estimation value reflects a higher uncertainty, which can be used to compel the lower-quality features to align with their higher-quality counterparts (Huang et al. 2023). The positions of these features are estimated by $\mathcal{P}_a^{r,h,w} = \mathbf{1} \odot \{U_a^{r,h,w} > U_b^{r,h,w}\}$.

Then, Mean Squared Error loss is utilized in loss function:

$$\mathcal{L}_{con,a} = \sum_{r \in \{4,8,16,32\}} \sum_{p \in \mathcal{P}_a^{r,h,w}} MSE(({}^r_a H^{de})^p, ({}^r_b H^{de})^p) \quad (10)$$

The total loss function of our HCS-TNAS is:

$$\mathcal{L}_{total,a} = \lambda_1 \mathcal{L}_{sup,a} + \lambda_2 \mathcal{L}_{uns,a} + \lambda_3 \mathcal{L}_{ind,a} + \lambda_4 \mathcal{L}_{con,a} \quad (11)$$

where $\mathcal{L}_{sup,a} = \frac{1}{2}[CE(p_{l,a}, y_{l,a}) + DICE(p_{l,a}, y_{l,a})]$ is the supervised loss, which is the combination of the cross-entropy loss and Dice loss calculated on the labeled dataset; $\mathcal{L}_{uns,a}$ refers to the unsupervised loss in Eq. (6); $\mathcal{L}_{ind,a}$ refers to the network independence loss in Eq. (7); $\mathcal{L}_{con,a}$ refers to contrastive loss in Eq. (10). $\lambda_1, \lambda_2, \lambda_3$ and λ_4 are hyper-parameters to balance the relationship between losses.

3.4 Stage-wise Optimization Strategy

To adapt to the hybrid constraint-driven SSL, we propose a stage-wise optimization strategy, summarized in Algorithm

1. In each iteration, we first fix the network parameters and optimize the combination matrix for E_B epochs. In the second stage, we fix the combination matrix and network architecture parameters and then update the network weights by minimizing \mathcal{L}_{total} . In the third stage, we only update the architecture parameters by minimizing \mathcal{L}_{total} after E_A epochs. During the optimization, continuous relaxation is implemented for the gradient descent algorithm.

Algorithm 1: Optimization Strategy

Input: Datasets $\mathcal{D}_l, \mathcal{D}_u$, weights w , architecture α, β, γ , combination matrices G_a, G_b , epochs E, E_A , and E_B .

Output: Searched $f(\theta_a^*), f(\theta_b^*)$.

- 1: **for** $e = 1, \dots, E$ **do**
 - 2: **for** $f = 1, \dots, E_B$ **do**
 - 3: Fix w, α, β, γ . Update G_a, G_b by maximizing $\mathcal{L}_{ind,a}$ and $\mathcal{L}_{ind,b}$, respectively.
 - 4: Fix G_a, G_b, α, γ . Update w, β of $f(\theta_a)$ and $f(\theta_b)$ by minimizing $\mathcal{L}_{total,a}$ and $\mathcal{L}_{total,b}$, respectively.
 - 5: **if** $e > E_A$ **then**
 - 6: Fix G_a, G_b, w, β . Update α, γ of $f(\theta_a)$ and $f(\theta_b)$ by minimizing $\mathcal{L}_{total,a}$ and $\mathcal{L}_{total,b}$, respectively.
-

4 Experiments

4.1 Datasets

To evaluate the effectiveness of our proposed HCS-TNAS method, three public datasets are utilized: (i) CAMUS dataset (Leclerc et al. 2019) is a large-scale 2D echocardiography dataset, comprising 2000 labeled images, and approximately 19000 unlabeled images. It includes four classes of labels: left ventricle endocardium (LV), left atrium, myocardium, and background. (ii) HMC-QU dataset (Kiranyaz et al. 2020) consists of 2D echocardiography videos. By splitting these sequences into individual images, a total of 4989 images are obtained, among which 2349 images are annotated with two classes of labels: left ventricle wall and background. (iii) CETUS dataset (Bernard et al. 2015) comprises 90 sequences of 3D ultrasound volumes. After randomly selecting 80 frames from each sequence, 7200 annotated images are obtained, with two classes of labels: LV and background. In our experiments, 3400 of these images are utilized as unlabeled data. More details on datasets and dataset partitioning methods are provided in Appendix C.1.

4.2 Experimental Settings

Network Architecture. In the encoder NAS, each cell has $N = 5$ intermediate nodes. For the resolution $r = 4$, the channel numbers are fixed as 8 for each node. When r doubles, the number of channels doubles accordingly. For partial channel connections, $\frac{1}{4}$ of the channels are allowed for searching. The default number of layers L is set to 8 and the default proportion of labeled data utilized is 50%.

Training Setup. The hyper-parameters $\lambda_1 = 1, \lambda_2 = \lambda_4 = 5 \exp(-5(1 - \frac{\min(i, I_{ramp})}{I_{ramp}})^2)$ are adopted following (Yu et al. 2019; Huang et al. 2023) at the i -th epoch,

Method	HMC-QU			CAMUS			CETUS		
	DSC \uparrow	IoU \uparrow	95HD \downarrow	DSC \uparrow	IoU \uparrow	95HD \downarrow	DSC \uparrow	IoU \uparrow	95HD \downarrow
UNet++	0.899 _{(0.005)*}	0.898 _{(0.004)*}	4.860 _{(0.102)*}	0.919 _{(0.006)*}	0.855 _{(0.009)*}	6.584 _{(0.578)*}	0.952 _{(0.002)*}	0.968 _{(0.001)*}	2.386 _{(0.091)*}
nnU-Net	0.908 _{(0.005)*}	0.907 _{(0.005)*}	3.843 _{(0.310)*}	0.922 _{(0.003)*}	0.860 _{(0.004)*}	6.075 _{(0.412)*}	0.958 _{(0.001)*}	0.970 _{(0.001)*}	2.099 _{(0.048)*}
Transfuse	0.903 _{(0.004)*}	0.903 _{(0.004)*}	4.304 _{(0.228)*}	0.923 _{(0.004)*}	0.861 _{(0.006)*}	5.853 _(0.496)	0.957 _{(0.002)*}	0.971 _{(0.001)*}	2.152 _{(0.102)*}
Auto-DeepLab	0.908 _{(0.004)*}	0.907 _{(0.004)*}	3.857 _{(0.164)*}	0.918 _{(0.003)*}	0.851 _{(0.006)*}	6.641 _{(0.473)*}	0.954 _{(0.004)*}	0.968 _{(0.001)*}	2.278 _{(0.133)*}
M ³ NAS	0.910 _{(0.007)*}	0.909 _{(0.006)*}	3.709 _{(0.288)*}	0.920 _{(0.004)*}	0.856 _{(0.004)*}	6.405 _{(0.556)*}	0.956 _{(0.005)*}	0.969 _{(0.004)*}	2.175 _{(0.174)*}
GeNAS	0.913 _{(0.004)*}	0.908 _{(0.005)*}	3.748 _{(0.219)*}	0.917 _{(0.003)*}	0.852 _{(0.003)*}	6.782 _{(0.425)*}	0.949 _{(0.002)*}	0.966 _{(0.001)*}	3.267 _{(0.119)*}
URPC \dagger	0.892 _{(0.004)*}	0.891 _{(0.004)*}	5.355 _{(0.125)*}	0.912 _{(0.002)*}	0.842 _{(0.002)*}	6.708 _{(0.152)*}	0.941 _{(0.004)*}	0.963 _{(0.003)*}	3.374 _{(0.185)*}
CPS \dagger	0.878 _{(0.005)*}	0.877 _{(0.005)*}	6.908 _{(0.296)*}	0.901 _{(0.004)*}	0.827 _{(0.005)*}	8.864 _{(0.477)*}	0.923 _{(0.005)*}	0.954 _{(0.003)*}	4.306 _{(0.282)*}
CnT-B \dagger	0.911 _{(0.006)*}	0.908 _{(0.005)*}	4.102 _{(0.496)*}	0.917 _{(0.003)*}	0.847 _{(0.002)*}	6.846 _{(0.421)*}	0.943 _{(0.004)*}	0.959 _{(0.003)*}	3.488 _{(0.341)*}
ARCO-SG \dagger	0.908 _{(0.003)*}	0.905 _{(0.004)*}	3.912 _{(0.203)*}	0.916 _{(0.004)*}	0.850 _{(0.003)*}	6.410 _{(0.494)*}	0.948 _{(0.005)*}	0.964 _{(0.004)*}	3.125 _{(0.282)*}
Se ² NAS \dagger	0.907 _{(0.004)*}	0.907 _{(0.004)*}	3.941 _{(0.303)*}	0.920 _{(0.002)*}	0.856 _{(0.003)*}	6.410 _{(0.311)*}	0.955 _{(0.003)*}	0.967 _{(0.003)*}	2.235 _{(0.111)*}
SSHNN \dagger	0.906 _{(0.002)*}	0.904 _{(0.002)*}	4.011 _{(0.145)*}	0.922 _{(0.002)*}	0.859 _{(0.003)*}	6.116 _{(0.278)*}	0.949 _{(0.002)*}	0.961 _{(0.001)*}	3.053 _{(0.087)*}
HCS-TNAS\dagger	0.933_(0.002)	0.931_(0.002)	2.480_(0.161)	0.937_(0.002)	0.884_(0.003)	5.042_(0.168)	0.972_(0.001)	0.978_(0.001)	1.620_(0.036)

Table 1: Comparison with SOTAs on public datasets. \dagger : SSL methods are tested under 50% annotations. The best and second results are highlighted in **bold** and underlined, respectively. * : $p < 0.01$ comparing against our method in each metric. Moreover, we test the generalization capability of HCS-TNAS on two additional datasets of other fields, shown in Appendix B.

Type	Method	Application Mode	DSC \uparrow	IoU \uparrow	95HD \downarrow	Params (M) \downarrow	FLOPs (G) \downarrow
Manual	TransUNet	Employ Transformer as Encoder	0.906 _{(0.003)*}	0.905 _{(0.004)*}	4.032 _{(0.207)*}	96.07	48.34
Manual	EfficientViT-L2	Multi-scale Tokens	0.916 _{(0.005)*}	0.915 _{(0.004)*}	3.356 _{(0.260)*}	52.12	91.45
Manual	ViT-H SAM	Employ Transformer as Encoder	0.920 _{(0.001)*}	0.918 _{(0.001)*}	3.093 _{(0.107)*}	636.00	246.20
NAS	Auto-DeepLab	No Transformer is Applied	0.908 _{(0.004)*}	0.907 _{(0.004)*}	3.857 _{(0.164)*}	44.42	347.52
NAS	SSHNN \dagger	Treat Transformer as Additional Branch	0.906 _{(0.002)*}	0.904 _{(0.002)*}	4.011 _{(0.145)*}	<u>38.82</u>	<u>52.78</u>
NAS	DAST	Treat Transformer as Candidate Operation	0.915 _{(0.002)*}	0.913 _{(0.002)*}	3.438 _{(0.119)*}	192.44	110.36
NAS	HCS-TNAS-E\dagger	Treat EfficientViT as Candidate Operation	0.923 _{(0.001)*}	0.922 _{(0.002)*}	2.884 _(0.123)	38.48	55.47
NAS	HCS-TNAS\dagger	Efficient NAS-ViT	0.933_(0.002)	0.931_(0.002)	2.480_(0.161)	41.20	67.50

Table 2: Discussion of various Transformer application modes on HMC-QU. \dagger : SSL methods are tested under 50% annotations.

where $I_{ramp} = 50$, and $\lambda_3 = 2$. The linear coefficient matrices G are optimized by Adam with a fixed learning rate of 0.001. The network weights w and architecture parameters β are optimized using SGD with an initial learning rate of 0.001, a momentum of 0.9, and a weight decay of 0.0003. For the architecture parameters α and γ , the Adam optimizer is applied with a learning rate of 0.003 and weight decay of 0.001. The total number of epochs is set to $E = 40$ and the architecture optimization begins at $E_A = 10$. In each epoch, G is updated $E_B = 6$ times. Experiments are conducted on an Nvidia A100 GPU and are repeated with 5 random seeds (42, 123, 512, 1026, 3407), where mean value and standard deviation are reported in $mean(std)$ format. For the impact of hyper-parameters, please refer to Appendix E.

Metrics. The Dice Similarity Coefficient (DSC), Intersection over Union (IoU), and 95% Hausdorff Distance (95HD). Wilcoxon signed-rank test is used to analyze statistical significance

Experimental Design. Our experiments are designed to answer the following research questions: 1) **RQ1**: How does HCS-TNAS perform compared to other SOTAs, and what is its generalization capability? (Sec. 4.3 and Appendix B); 2) **RQ2**: How effective is each component of HCS-TNAS, and is the NAS modification made to ViT reasonable? (Sec. 4.4); 3) **RQ3**: How does HCS-TNAS perform with fewer

labeled samples? (Sec. 4.4); 4) **RQ4**: How does HCS-TNAS perform in terms of search cost? (Sec. 4.5).

4.3 Comparison with SOTA Methods

We evaluate HCS-TNAS against other SOTAs, including supervised handcrafts: UNet++ (Zhou et al. 2019), nnU-Net (Isensee et al. 2021), Transfuse (Zhang, Liu, and Hu 2021); supervised NAS: Auto-DeepLab (Liu et al. 2019), M³NAS (Lu et al. 2022), GeNAS (Jeong et al. 2023); semi-supervised handcrafts: URPC (Luo et al. 2021), CPS (Chen et al. 2021b), CnT-B (Huang et al. 2023), ARCO-SG (You et al. 2024); and semi-supervised NAS: Se²NAS (Pauletto, Amini, and Winckler 2022), SSHNN (Chen et al. 2024).

Table 1 presents the quantitative results of various methods on HMC-QU, CAMUS, and CETUS. SSL methods are trained using 50% of annotated data, while supervised methods use 100% of annotated data without utilizing unlabeled data. It can be observed that HCS-TNAS achieves the best results across all evaluation metrics. On HMC-QU, HCS-TNAS outperforms the original SOTA method (CnB-T) by 2.2% in DSC, 2.3% in IoU, and 1.622 in 95HD, while it also achieves superior performance on the other two datasets.

4.4 Ablation Studies

Effects of Sub-modules. To analyze the effects of each sub-module, experiments are conducted in Table 3. The

No.	NAS	\mathcal{L}_{uns}	\mathcal{L}_{ind}	\mathcal{L}_{con}	DSC \uparrow	IoU \uparrow	95HD \downarrow
1	✗	✗	✗	✗	0.905 _(0.002)	0.906 _(0.003)	4.310 _(0.204)
2	✓	✗	✗	✗	0.912 _(0.001)	0.911 _(0.002)	3.623 _(0.131)
3	✗	✓	✗	✗	0.910 _(0.001)	0.910 _(0.001)	3.674 _(0.100)
4	✗	✓	✓	✗	0.919 _(0.001)	0.920 _(0.002)	3.058 _(0.093)
5	✗	✓	✗	✓	0.917 _(0.003)	0.915 _(0.002)	3.356 _(0.297)
6	✓	✓	✗	✗	0.919 _(0.002)	0.918 _(0.002)	3.041 _(0.165)
7	✓	✓	✓	✗	0.926 _(0.002)	0.925 _(0.001)	2.752 _(0.102)
8	✓	✓	✓	✓	0.933 _(0.002)	0.931 _(0.002)	2.480 _(0.161)

Table 3: Ablation studies of each component in HCS-TNAS structure on HMC-QU. ‘‘NAS’’ denotes our proposed Efficient NAS-ViT. More experiments on the other two datasets are shown in Appendix D.1.

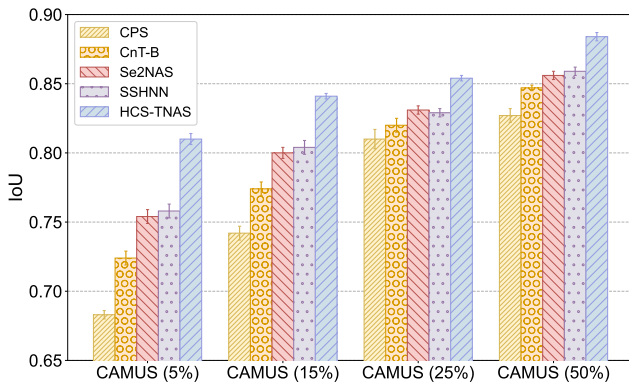


Figure 4: The impact of annotation proportions on SOTAs is tested on CAMUS. HCS-TNAS shows its robustness.

baseline model (No. 1) is the NAS backbone (Sec 3.2) without the Efficient NAS-ViT module, trained using 50% of the annotated data. Firstly, incorporating the Efficient NAS-ViT module improves the segmentation performance from a DSC of 0.905 to 0.912, consistent with the expectation of enhancing the context extraction capabilities. After introducing the co-training SSL framework (No. 6), HCS-TNAS obtains 0.7% improvements, attributed to the additional information gained from the unlabeled data. Furthermore, when the network independence loss is considered (No. 7), there are 9.5% 95HD increments over the previous version (No. 6). The effectiveness of contrastive learning is validated in No. 5, which improves the performance by 0.7% in DSC compared to independently using the \mathcal{L}_{uns} in No. 3.

Effects of Transformer Application Modes. Table 2 presents an assessment of SOTAs employing various Transformer application modes on HMC-QU. TransUNet (Chen et al. 2021a) and SAM (Kirillov et al. 2023) use ViTs as the encoder. EfficientViT-L2 (Cai et al. 2023) uses fixed multi-scale tokens within the ViT. Auto-DeepLab is a NAS model that does not apply the Transformer. SSHNN adopts ViTs as an additional branch. DAST directly uses the ViT as a candidate operation during the network search process. In the HCS-TNAS-E, we also evaluated the case where Ef-

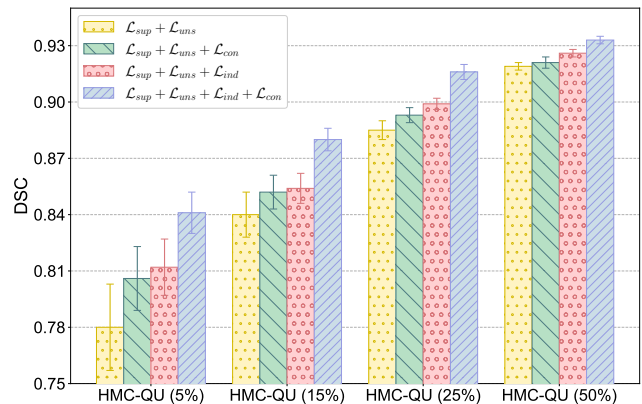


Figure 5: Sensitivity analysis of hybrid constraints. The case considering additional constraints shows better robustness.

ficientViT was treated as a candidate operation instead of employing the Efficient NAS-ViT. While maintaining the highest accuracy, our method has a smaller model scale and lower FLOPs. Moreover, the results of the HCS-TNAS-E variant clearly show that the Transformer application mode significantly impacts model performance.

Impact of the Annotation Ratio. Fig. 4 elaborates the results of representative SSL networks and HCS-TNAS with varying proportions of annotations on CAMUS. It can be observed that HCS-TNAS performs more stable than other advanced SSL methods. When the annotation ratio descends from 50% to 5%, the IoU of CPS, CnT-B, Se²NAS, and SSHNN drops by 14.4%, 12.3%, 10.2%, and 10.1%, respectively. However, the IoU of HCS-TNAS only decreases by 7.4%, verifying its robustness. We attribute this achievement to the hybrid constraint-driven SSL approach, which enhances the utilization of limited data.

Analysis of Hybrid Constraints. We investigate whether algorithmic independence loss \mathcal{L}_{ind} or contrastive loss \mathcal{L}_{con} would impact its performance under varying annotation ratios on HMC-QU, presented in Fig. 5. When both \mathcal{L}_{ind} and \mathcal{L}_{con} are not considered, there is a 13.9% drop in DSC as the annotation ratio decreases from 50% to 5%, which is larger

than the 11.4% and 11.5% DSC decreases observed when \mathcal{L}_{con} or \mathcal{L}_{ind} is excluded, respectively. Notably, the DSC of HCS-TNAS decreases by 9.2%, representing the smallest drop among these cases. Results show that (1) \mathcal{L}_{ind} encourages the creation of complementary networks that assist in training by providing multi-view information from the same data; (2) \mathcal{L}_{con} considers feature-level uncertainty where regions with lower uncertainty are filtered out, which is helpful for stable training under limited annotations.

4.5 Search Cost Analysis

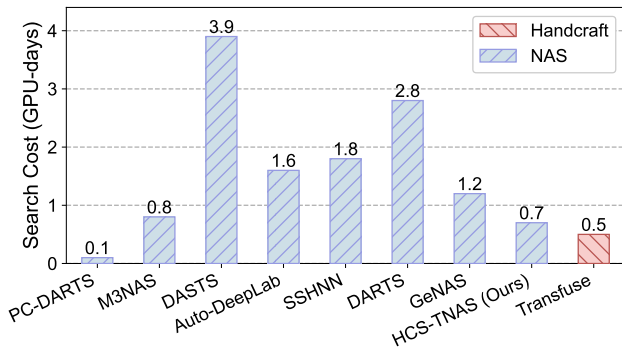


Figure 6: Comparison of search cost with SOTAs.

In Fig. 6, we compare the required architecture search time of HCS-TNAS with an advanced handcrafted model Transfuse (performance is shown in Table 1) and other NAS frameworks on the HMC-QU dataset. The search cost for TransFuse is based on training time, while for NAS models, it includes both training and search time on an Nvidia A100 GPU. Our method currently takes 0.7 GPU days to train the model, where the search has become less time-consuming and even competitive compared to the handcraft.

5 Conclusion

In this paper, we propose a hybrid constraint-driven semi-supervised Transformer-NAS to address two key challenges in ultrasound image segmentation: optimize multi-scale feature representation and mitigate data dependency. For the first issue, HCS-TNAS implements a three-level search, coupled with the Efficient NAS-ViT to enhance contextual feature extraction. For the second issue, we propose a hybrid constraint-driven SSL framework to boost the model under limited annotations. Extensive experiments on public datasets prove the effectiveness of the proposed method.

References

Bai, W.; Oktay, O.; Sinclair, M.; Suzuki, H.; Rajchl, M.; Tarroni, G.; Glocker, B.; King, A.; Matthews, P. M.; and Rueckert, D. 2017. Semi-supervised learning for network-based cardiac MR image segmentation. In *Medical Image Computing and Computer-Assisted Intervention- MICCAI 2017: 20th International Conference, Quebec City, QC, Canada, September 11-13, 2017, Proceedings, Part II 20*, 253–260. Springer.

Bernard, O.; Bosch, J. G.; Heyde, B.; Alessandrini, M.; Barbosa, D.; Camarasu-Pop, S.; Cervenansky, F.; Valette, S.; Mirea, O.; Bernier, M.; et al. 2015. Standardized evaluation system for left ventricular segmentation algorithms in 3D echocardiography. *IEEE transactions on medical imaging*, 35(4): 967–977.

Bernard, O.; Lalande, A.; Zotti, C.; Cervenansky, F.; Yang, X.; Heng, P.-A.; Cetin, I.; Lekadir, K.; Camara, O.; Ballester, M. A. G.; et al. 2018. Deep learning techniques for automatic MRI cardiac multi-structures segmentation and diagnosis: is the problem solved? *IEEE transactions on medical imaging*, 37(11): 2514–2525.

Cai, H.; Li, J.; Hu, M.; Gan, C.; and Han, S. 2023. Efficientvit: Lightweight multi-scale attention for high-resolution dense prediction. In *Proceedings of the IEEE/CVF International Conference on Computer Vision*, 17302–17313.

Chen, J.; Lu, Y.; Yu, Q.; Luo, X.; Adeli, E.; Wang, Y.; Lu, L.; Yuille, A. L.; and Zhou, Y. 2021a. Transunet: Transformers make strong encoders for medical image segmentation. *arXiv preprint arXiv:2102.04306*.

Chen, R.; Luo, J.; Nian, F.; Cen, Y.; Peng, Y.; and Yu, Z. 2024. SSHNN: Semi-Supervised Hybrid NAS Network for Echocardiographic Image Segmentation. In *ICASSP 2024-2024 IEEE International Conference on Acoustics, Speech and Signal Processing (ICASSP)*, 1541–1545. IEEE.

Chen, X.; Yuan, Y.; Zeng, G.; and Wang, J. 2021b. Semi-supervised semantic segmentation with cross pseudo supervision. In *Proceedings of the IEEE/CVF Conference on Computer Vision and Pattern Recognition*, 2613–2622.

Codella, N. C.; Gutman, D.; Celebi, M. E.; Helba, B.; Marchetti, M. A.; Dusza, S. W.; Kallou, A.; Liopyris, K.; Mishra, N.; Kittler, H.; et al. 2018. Skin lesion analysis toward melanoma detection: A challenge at the 2017 international symposium on biomedical imaging (isbi), hosted by the international skin imaging collaboration (isic). In *2018 IEEE 15th international symposium on biomedical imaging (ISBI 2018)*, 168–172. IEEE.

Dosovitskiy, A.; Beyer, L.; Kolesnikov, A.; Weissenborn, D.; Zhai, X.; Unterthiner, T.; Dehghani, M.; Minderer, M.; Heigold, G.; Gelly, S.; et al. 2020. An image is worth 16x16 words: Transformers for image recognition at scale. *arXiv preprint arXiv:2010.11929*.

Huang, H.; Huang, Y.; Xie, S.; Lin, L.; Ruofeng, T.; Chen, Y.-w.; Li, Y.; and Zheng, Y. 2023. Semi-Supervised Convolutional Vision Transformer with Bi-Level Uncertainty Estimation for Medical Image Segmentation. In *Proceedings of the 31st ACM International Conference on Multimedia*, 5214–5222.

Isensee, F.; Jaeger, P. F.; Kohl, S. A.; Petersen, J.; and Maier-Hein, K. H. 2021. nnU-Net: a self-configuring method for deep learning-based biomedical image segmentation. *Nature methods*, 18(2): 203–211.

Jeong, J.; Yu, J.; Park, G.; Han, D.; and Yoo, Y. 2023. GenAS: neural architecture search with better generalization. *arXiv preprint arXiv:2305.08611*.

- Kiranyaz, S.; Degerli, A.; Hamid, T.; Mazhar, R.; Ahmed, R. E. F.; Abouhasera, R.; Zabihi, M.; Malik, J.; Hamila, R.; and Gabbouj, M. 2020. Left ventricular wall motion estimation by active polynomials for acute myocardial infarction detection. *IEEE Access*, 8: 210301–210317.
- Kirillov, A.; Mintun, E.; Ravi, N.; Mao, H.; Rolland, C.; Gustafson, L.; Xiao, T.; Whitehead, S.; Berg, A. C.; Lo, W.-Y.; et al. 2023. Segment anything. In *Proceedings of the IEEE/CVF International Conference on Computer Vision*, 4015–4026.
- Leclerc, S.; Smistad, E.; Pedrosa, J.; Østvik, A.; Cervenansky, F.; Espinosa, F.; Espeland, T.; Berg, E. A. R.; Jodoin, P.-M.; Grenier, T.; et al. 2019. Deep learning for segmentation using an open large-scale dataset in 2D echocardiography. *IEEE transactions on medical imaging*, 38(9): 2198–2210.
- Liu, C.; Chen, L.-C.; Schroff, F.; Adam, H.; Hua, W.; Yuille, A. L.; and Fei-Fei, L. 2019. Auto-deeplab: Hierarchical neural architecture search for semantic image segmentation. In *Proceedings of the IEEE/CVF conference on computer vision and pattern recognition*, 82–92.
- Liu, H.; Simonyan, K.; and Yang, Y. 2018. Darts: Differentiable architecture search. *arXiv preprint arXiv:1806.09055*.
- Lu, Z.; Xia, W.; Huang, Y.; Hou, M.; Chen, H.; Zhou, J.; Shan, H.; and Zhang, Y. 2022. M³ NAS: Multi-scale and multi-level memory-efficient neural architecture search for low-dose CT denoising. *IEEE Transactions on Medical Imaging*, 42(3): 850–863.
- Luo, X.; Liao, W.; Chen, J.; Song, T.; Chen, Y.; Zhang, S.; Chen, N.; Wang, G.; and Zhang, S. 2021. Efficient semi-supervised gross target volume of nasopharyngeal carcinoma segmentation via uncertainty rectified pyramid consistency. In *Medical Image Computing and Computer Assisted Intervention–MICCAI 2021: 24th International Conference, Strasbourg, France, September 27–October 1, 2021, Proceedings, Part II 24*, 318–329. Springer.
- Miao, J.; Chen, C.; Liu, F.; Wei, H.; and Heng, P.-A. 2023. CauSSL: Causality-inspired Semi-supervised Learning for Medical Image Segmentation. In *Proceedings of the IEEE/CVF International Conference on Computer Vision*, 21426–21437.
- Pauletto, L.; Amini, M.-R.; and Winckler, N. 2022. Se² NAS: Self-Semi-Supervised architecture optimization for Semantic Segmentation. In *2022 26th International Conference on Pattern Recognition (ICPR)*, 54–60. IEEE.
- Qiao, S.; Shen, W.; Zhang, Z.; Wang, B.; and Yuille, A. 2018. Deep co-training for semi-supervised image recognition. In *Proceedings of the european conference on computer vision (eccv)*, 135–152.
- Ronneberger, O.; Fischer, P.; and Brox, T. 2015. U-net: Convolutional networks for biomedical image segmentation. In *Medical Image Computing and Computer-Assisted Intervention–MICCAI 2015: 18th International Conference, Munich, Germany, October 5-9, 2015, Proceedings, Part III 18*, 234–241. Springer.
- Tarvainen, A.; and Valpola, H. 2017. Mean teachers are better role models: Weight-averaged consistency targets improve semi-supervised deep learning results. *Advances in neural information processing systems*, 30.
- Wang, G.; Zhai, S.; Lasio, G.; Zhang, B.; Yi, B.; Chen, S.; Macvittie, T. J.; Metaxas, D.; Zhou, J.; and Zhang, S. 2021. Semi-supervised segmentation of radiation-induced pulmonary fibrosis from lung CT scans with multi-scale guided dense attention. *IEEE transactions on medical imaging*, 41(3): 531–542.
- Xia, Y.; Yang, D.; Yu, Z.; Liu, F.; Cai, J.; Yu, L.; Zhu, Z.; Xu, D.; Yuille, A.; and Roth, H. 2020. Uncertainty-aware multi-view co-training for semi-supervised medical image segmentation and domain adaptation. *Medical image analysis*, 65: 101766.
- Xu, Y.; Xie, L.; Zhang, X.; Chen, X.; Qi, G.-J.; Tian, Q.; and Xiong, H. 2019. Pc-darts: Partial channel connections for memory-efficient architecture search. *arXiv preprint arXiv:1907.05737*.
- Yang, D.; Xu, Z.; He, Y.; Nath, V.; Li, W.; Myronenko, A.; Hatamizadeh, A.; Zhao, C.; Roth, H. R.; and Xu, D. 2023. DAST: Differentiable Architecture Search with Transformer for 3D Medical Image Segmentation. In *International Conference on Medical Image Computing and Computer-Assisted Intervention*, 747–756. Springer.
- You, C.; Dai, W.; Min, Y.; Liu, F.; Clifton, D.; Zhou, S. K.; Staib, L.; and Duncan, J. 2024. Rethinking semi-supervised medical image segmentation: A variance-reduction perspective. *Advances in neural information processing systems*, 36.
- Yu, L.; Wang, S.; Li, X.; Fu, C.-W.; and Heng, P.-A. 2019. Uncertainty-aware self-ensembling model for semi-supervised 3D left atrium segmentation. In *Medical Image Computing and Computer Assisted Intervention–MICCAI 2019: 22nd International Conference, Shenzhen, China, October 13–17, 2019, Proceedings, Part II 22*, 605–613. Springer.
- Yu, Z.; Lee, F.; and Chen, Q. 2023. HCT-net: hybrid CNN-transformer model based on a neural architecture search network for medical image segmentation. *Applied Intelligence*, 1–17.
- Zhang, Y.; Liu, H.; and Hu, Q. 2021. Transfuse: Fusing transformers and cnns for medical image segmentation. In *Medical Image Computing and Computer Assisted Intervention–MICCAI 2021: 24th International Conference, Strasbourg, France, September 27–October 1, 2021, Proceedings, Part I 24*, 14–24. Springer.
- Zhou, G.-Q.; Zhang, W.-B.; Shi, Z.-Q.; Qi, Z.-R.; Wang, K.-N.; Song, H.; Yao, J.; and Chen, Y. 2023. DSANet: Dual-branch Shape-Aware Network for Echocardiography Segmentation in Apical Views. *IEEE Journal of Biomedical and Health Informatics*.
- Zhou, Z.; Siddiquee, M. M. R.; Tajbakhsh, N.; and Liang, J. 2019. Unet++: Redesigning skip connections to exploit multiscale features in image segmentation. *IEEE transactions on medical imaging*, 39(6): 1856–1867.

Supplementary Material

In the supplementary material, we provide additional details and experimental results to enhance the understanding and insights into our proposed HCS-TNAS. This supplementary material is organized as:

- In Sec. A, a more detailed description of the role of architecture parameters for the NAS backbone. The candidate operations used in the encoder and decoder cell searches are shown.
- In Sec. B, we test the generalization capability of our proposed HCS-TNAS compared with previous SOTA methods on two additional medical image datasets from another field.
- In Sec. C, We provide more details about the employed datasets and a comprehensive analysis of the experimental results from the perspectives of visualization results, training convergence, and proportions of candidate operations in the final searched architecture, respectively, having a deeper insight into the structure design.
- In Sec. D, we present additional ablation studies, analyzing the effects of each sub-module in HCS-TNAS on more datasets, various candidate operation sets in the search process, and different feature resolutions used in the training constraint, respectively.
- In Sec. E, we present additional hyper-parameter studies, discussing how loss coefficients influence the constraint balance and the impact of the network size.
- In Sec. F, we discuss the potential for model improvements and our future research directions.

Candidate Operations	Encoder	Decoder
3×3 separable convolution	✓	✓
5×5 separable convolution	✓	✓
3×3 convolution with dilation rate 2	✓	✓
5×5 convolution with dilation rate 2	✓	✓
3×3 average/max pooling	✓	✗
skip connection	✓	✓
no connection (zero)	✓	✗

Table 4: Encoder cell and decoder cell candidate operations, where different candidate operations are considered according to their respective roles. The rationality of the design will be discussed in Sec. C.4.

A More Details about HCS-TNAS

As we introduced in the Sec. “Methodology” of the main paper, the architecture parameters α and γ are responsible for updating the candidate operations in the encoder and decoder cells, respectively. In HCS-TNAS, to enlarge the search space, unlike existing works where all cells share

the same architecture parameters, our architecture parameters α for encoder cells are defined as a 3-dimensional tuple ($Cell, Edge, Operation$), and γ for decoder cells is defined as a 2-dimensional tuple ($Cell, Operation$).

- $Cell$ indicates that different cells are optimized by specialized parameters, overcoming the limitation of a simple cell type, and enabling a larger search space to be explored.
- $Edge$ represents the connection between each intermediate node within a cell, which is used for feature aggregation at the intermediate nodes. Note that the decoder cell does not have this parameter to reduce the parameter count and training time.
- $Operation$ denotes the number of operation types. As shown in Table 4, 8 different choices are provided for the encoder to ensure diversity in the selection, while 5 different choices are provided for the decoder. The encoder and decoder have different sets of candidate operations. The rationale behind designing different candidate operation sets will be discussed in more ablation studies.

Thus, in the search process for the encoder and decoder cells, we allow different cells to have different structures, and different node-to-node connections to have different operations. This approach enables the network to have a vast search space and optimization potential without requiring a large number of layers.

B Generalization Capability

Method	Publication	ISIC (10%)		ISIC (15%)	
		DSC	95HD	DSC	95HD
CPS	CVPR’21	0.746	15.722	0.779	12.910
CnT-B	ACMMM’23	0.790	11.879	0.814	9.583
ARCO-SG	NeurIPS’23	<u>0.798</u>	<u>11.352</u>	<u>0.816</u>	9.600
SSHNN	ICASSP’24	0.788	12.064	0.809	10.119
HCS-TNAS	/	0.817	9.024	0.840	7.391

Table 5: Comparison with SOTA methods on ISIC under different ratios of annotations to verify the generalization capability of HCS-TNAS.

Method	Publication	ACDC (10%)		ACDC (15%)	
		DSC	95HD	DSC	95HD
CPS	CVPR’21	0.831	10.621	0.851	7.304
CnT-B	ACMMM’23	<u>0.876</u>	<u>5.120</u>	0.894	2.853
ARCO-SG	NeurIPS’23	0.872	6.144	<u>0.896</u>	<u>2.607</u>
SSHNN	ICASSP’24	0.868	6.722	0.889	3.519
HCS-TNAS	/	0.890	3.356	0.915	1.677

Table 6: Comparison with SOTA methods on ACDC under different ratios of annotations to verify the generalization capability of HCS-TNAS.

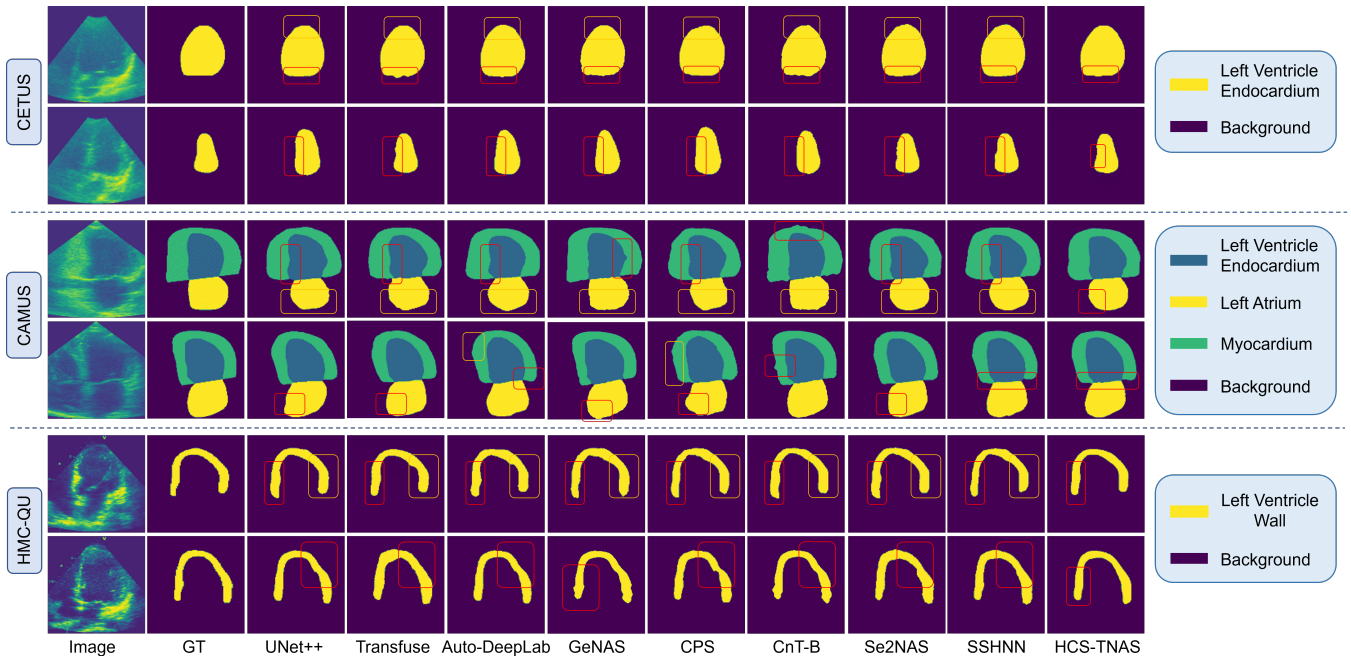


Figure 7: Visualization of segmentation results obtained by our proposed HCS-TNAS and other SOTA methods on the CETUS, CAMUS, and HMC-QU datasets. Note that Resize and crop operations are applied to the model’s predictions to visualize their segmentation differences. Red or orange boxes are used to highlight obvious wrong predictions, showing that our method has fewer over-segmentation and under-segmentation issues, yielding segmented shapes that closely match expert annotations.

To test the generalization capability of HCS-TNAS, we further conduct experiments on the International Skin Imaging Collaboration (ISIC) (Codella et al. 2018) dataset and Automated Cardiac Diagnosis Challenge (ACDC) (Bernard et al. 2018). (1) The ISIC dataset is a skin lesion segmentation dataset comprising 2594 dermoscopy images, with 1838 training images and 756 validation images. (2) The ACDC dataset is a magnetic resonance imaging scan dataset that includes 100 scans of three organs. Following (Huang et al. 2023), we use 70 samples for training and 30 samples for testing. All images are resized to 224×224 pixels. For a semi-supervised setting, 10% and 15% training data are labeled, while the rest training data are unlabeled.

As shown in Table 5 and Table 6, we evaluate our method against other SOTAs, including CPS (Chen et al. 2021b), CnT-B (Huang et al. 2023), ARCO-SG (You et al. 2024), and SSHNN (Chen et al. 2024). Our method achieves the best segmentation performance in all semi-supervised settings (10% and 15%), on the ICIC dataset, with the improvements of DSC: 1.9%, 2.4%, and 95HD: -2.328mm, -2.209mm over the runner-up; on the ACDC dataset, with the improvements of DSC: 1.4%, 1.9%, and 95HD: -1.764mm, -0.930mm over the runner-up. Extensive results demonstrate the generalization capability of our proposed model.

C More Experimental Results

C.1 Dataset Details

CAMUS Dataset. The CAMUS dataset (Leclerc et al. 2019) is a large open 2D echocardiography dataset collected

from 500 patients. Each patient contributes a 4-chamber and a 2-chamber view sequence, each containing approximately 20 unlabeled images. Exceptions are made for annotations at the moments of end-diastole (ED) and end-systole (ES). Thus, there are 2000 labeled images and approximately 19000 unlabeled images. The segmentation labels include four categories: the left ventricle endocardium, the myocardium, the left atrium, and the background. All images are resized to 224×224 pixels for training.

HMC-QU Dataset. The HMC-QU dataset (Kiranyaz et al. 2020) is composed of 2D echocardiography videos from the apical 4-chamber (A4C) and apical 2-chamber (A2C) views. In a specific subset of the HMC-QU dataset, 109 A4C view echocardiography recordings from 72 myocardial infarction (MI) patients and 37 non-MI subjects are annotated for one cardiac cycle. The remaining frames are unlabeled. Through the statistical analysis, the HMC-QU dataset consists of 4989 images in total, with 2349 images labeled for two categories: the left ventricle wall and the background. All images are resized to 192×192 pixels for training.

CETUS Dataset. The CETUS dataset (Bernard et al. 2015) comprises 90 sequences (both ED and ES) of 3D ultrasound volumes capturing one complete cardiac cycle, collected from 45 patients. It can be categorized into three subgroups: 15 healthy individuals, 15 patients with a history of myocardial infarction at least 3 months prior to data acquisition, and 15 patients with dilated cardiomyopathy. To address the non-uniform duration of left ventricle endo-

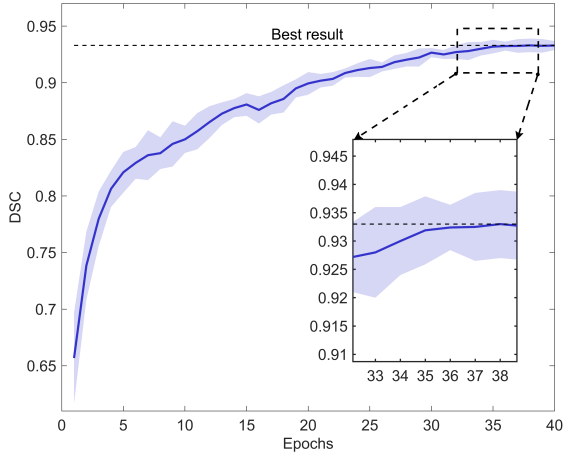


Figure 8: Validation accuracy during 40 epochs of architecture search optimization across 5 random trials on the HMC-QU dataset. It can be seen that the curve steadily rises and can converge.

cardium presence and ensure fairness, we randomly selected 80 frames from each sequence to form the dataset. Consequently, the selection process provides 7200 labeled images, all resized to 192×192 pixels. The ground-truth mask consists of two distinct labels: the left ventricle endocardium and the background.

Dataset Partitioning Approach. For the CAMUS dataset, the training and test sets comprise 1800 and 200 labeled images, respectively, while for the CETUS dataset, they comprise 3400 and 400 labeled images, and for the HMC-QU dataset, they comprise 2000 and 349 labeled images. For the SSL experiments with HCS-TNAS on the CAMUS dataset, we randomly selected 90, 270, 450, and 900 images from the training set, corresponding to 5%, 15%, 25%, and 50% labeled data, respectively, while using 19432 unlabeled images for training. On the CETUS dataset, we randomly selected 170, 510, 850, and 1700 images from the training set, corresponding to 5%, 15%, 25%, and 50% labeled data, respectively, and used 3400 unlabeled images for training. For the HMC-QU dataset, 100, 300, 500, and 1000 images are randomly selected as 5%, 15%, 25%, and 50% labeled data, respectively, while 2640 unlabeled images are used for training.

C.2 Visualization Results

Fig. 7 elaborates the qualitative results of our proposed HCS-TNAS against previous SOTA methods on the CETUS, CAMUS, and HMC-QU datasets. It can be observed that our method mitigates over and under-segmentation issues, and exhibits smoother boundaries between different labels. Overall, our proposed HCS-TNAS achieves better segmentation results.

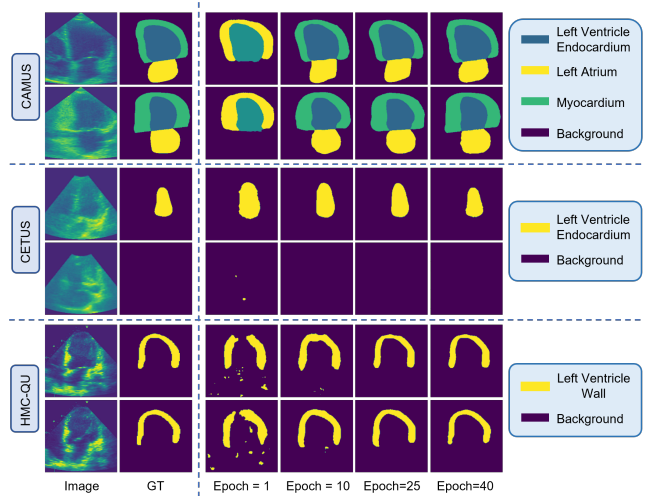


Figure 9: Qualitative assessment of the segmentation performance of HCS-TNAS throughout the training process. It can be observed that as the number of training iterations increases, the segmentation results gradually approach expert annotations.

C.3 Convergence Behavior

Fig. 8 depicts the validation accuracy trajectory over 40 epochs during the architecture search optimization process in the metric of DSC. We present our experimental results across 5 random trials on the HMC-QU dataset using 50% labeled data. While the deep blue curve represents the mean validation accuracy, the light blue shaded region around it suggests variability across trials. The validation accuracy curve exhibits an initial steep ascent, followed by a more gradual increase, ultimately converging close to 0.933. An inset magnifies the changes of the curve at final epochs, revealing minor fluctuations within a tight range during terminal convergence and presenting stability after 37 epochs. We also experimented with searching for longer epochs (50, 60, 70), but did not observe any significant benefit.

Fig. 9 illustrates the progressive refinement of segmentation predictions during the training process of the HCS-TNAS for ultrasound image segmentation on the CAMUS, CETUS, and HMC-QU datasets, offering an instructive portrayal of the model’s progressive enhancement in this clinically significant application.

C.4 Analysis on Candidate Operation Proportion

As mentioned previously, we have defined that the cells within both the encoder and decoder architectures possess their distinct architecture parameters rather than sharing them. To gain a deeper insight into the final architecture, the statistical distributions of candidate operations in the final searched encoder and decoder architecture on three datasets (CAMUS, CETUS, and HMC-QU) are presented in Fig. 10 through Fig. 15, where the compositions of operations within the encoder and decoder cells are individually characterized.

The proportion of each candidate operation in the encoder and decoder cells is calculated as follows:

$$P_{O_k \in \mathcal{O}^{en}} = \frac{\sum_{i=1}^{\sum Cells} \sum_{j=1}^{\sum Edges} \alpha_{i,j,O_k}}{\sum Cells \sum Edges} \quad (12)$$

and

$$P_{O_k \in \mathcal{O}^{de}} = \frac{\sum_{i=1}^{\sum Cells} \alpha_{i,O_k}}{\sum Cells} \quad (13)$$

where $\sum Cells$ denotes the total number of the encoder or decoder cells, and $\sum Edges$ denotes the total number of node-to-node edges in the encoder. \mathcal{O}^{en} and \mathcal{O}^{de} represent the sets of candidate operations for the encoder and decoder, respectively.

By comparing the two charts (encoder and decoder) for each dataset, it can be observed that while the decoder favors skip connections and a more diverse set of convolution operations, the encoder places greater emphasis on separable convolutions and also includes pooling operations. Specifically, the decoder architecture searched by NAS has a much higher proportion of dilated convolutions compared to the encoder architecture. This distinction in operation distributions between the decoder and encoder components likely reflects their respective roles and computational requirements within the overall architecture, with the decoder emphasizing skip connections and diverse convolutions for up-sampling and feature synthesis, while the encoder focuses on efficient feature extraction through separable convolutions and pooling operations.

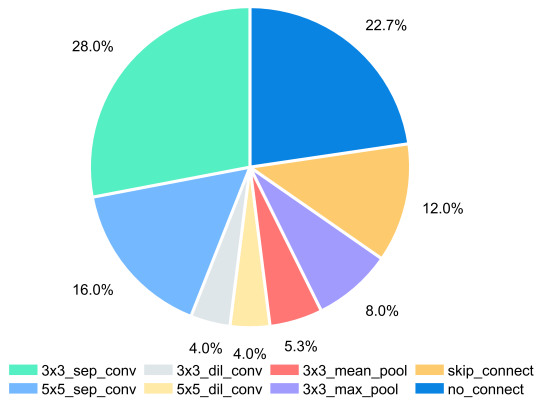


Figure 10: The proportion of each candidate operation in the cells of the encoder NAS of the final searched network on the HMC-QU dataset.

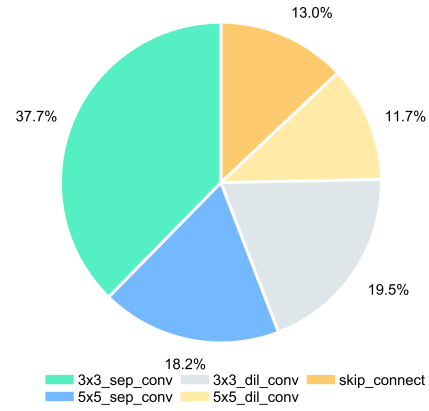


Figure 11: The proportion of each candidate operation in the cells of the decoder NAS of the final searched network on the HMC-QU dataset.

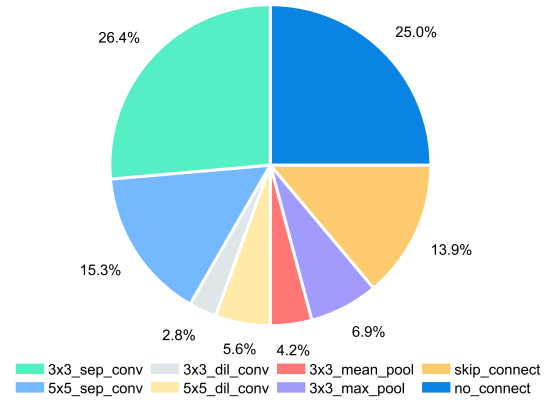


Figure 12: The proportion of each candidate operation in the cells of the encoder NAS of the final searched network on the CAMUS dataset.

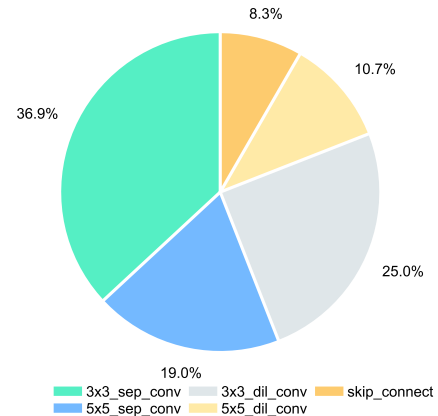


Figure 13: The proportion of each candidate operation in the cells of the decoder NAS of the final searched network on the CAMUS dataset.

No.	Efficient NAS-ViT	\mathcal{L}_{uns}	\mathcal{L}_{ind}	\mathcal{L}_{con}	CAMUS (50%)			CETUS (50%)		
					DSC \uparrow	IoU \uparrow	95HD \downarrow	DSC \uparrow	IoU \uparrow	95HD \downarrow
1	✗	✗	✗	✗	0.918 _(0.003)	0.854 _(0.003)	6.587 _(0.440)	0.951 _(0.005)	0.967 _(0.004)	2.357 _(0.196)
2	✓	✗	✗	✗	0.924 _(0.004)	0.860 _(0.007)	5.924 _(0.566)	0.959 _(0.002)	0.969 _(0.002)	2.049 _(0.099)
3	✗	✓	✗	✗	0.923 _(0.002)	0.860 _(0.003)	6.024 _(0.313)	0.959 _(0.002)	0.970 _(0.001)	2.064 _(0.103)
4	✗	✓	✓	✗	0.930 _(0.003)	0.871 _(0.004)	5.329 _(0.277)	0.962 _(0.001)	0.974 _(0.001)	1.926 _(0.051)
5	✗	✓	✗	✓	0.927 _(0.005)	0.864 _(0.006)	5.509 _(0.501)	0.960 _(0.003)	0.971 _(0.002)	2.011 _(0.148)
6	✓	✓	✗	✗	0.929 _(0.002)	0.869 _(0.002)	5.395 _(0.264)	0.963 _(0.002)	0.975 _(0.002)	1.903 _(0.115)
7	✓	✓	✓	✗	0.934 _(0.001)	0.879 _(0.002)	5.205 _(0.189)	0.968 _(0.001)	0.977 _(0.001)	1.788 _(0.047)
8	✓	✓	✓	✓	0.937_(0.002)	0.884_(0.003)	5.042_(0.168)	0.972_(0.001)	0.978_(0.001)	1.620_(0.036)

Table 7: Ablation studies of each component in the proposed network structure on HMC-QU, CAMUS, and CETUS datasets.

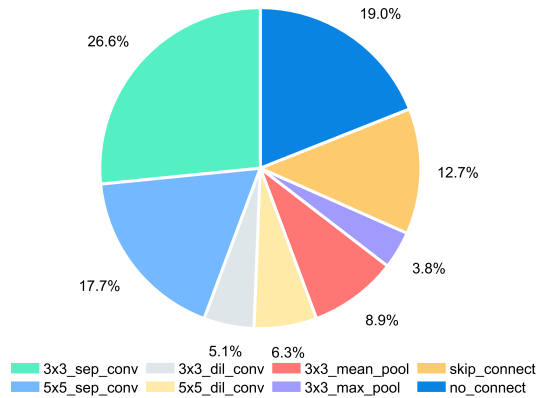


Figure 14: The proportion of each candidate operation in the cells of the encoder NAS of the final searched network on the CETUS dataset.

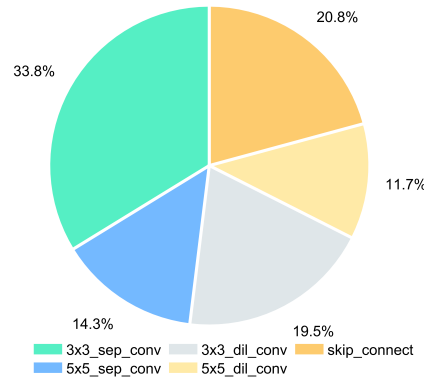


Figure 15: The proportion of each candidate operation in the cells of the decoder NAS of the final searched network on the CETUS dataset.

D More Ablation Studies

D.1 Effects of Sub-modules

To analyze the effects of each sub-module, additional experiments on CAMUS and CETUS are conducted in Table 7. The baseline model (No. 1) is the NAS backbone (Sec 3.2) without the Efficient NAS-ViT module, trained using 50% of the annotated data. Firstly, incorporating the Efficient NAS-ViT module improves the segmentation performance from a DSC of 0.918 to 0.924 on the CAMUS dataset, consistent with the expectation of enhancing the context extraction capabilities. After introducing the co-training algorithm as the SSL framework (No. 6), HCS-TNAS obtains 0.5% and 0.4% DSC improvements on CAMUS and CETUS, respectively, attributed to the additional information gained from the unlabeled data facilitated by the SSL. Furthermore, when the network independence loss is considered (No. 7), there are 3.52% and 6.04% 95HD increments over the previous version (No. 6) on the two datasets respectively. The effectiveness of contrastive learning is validated in No. 5, which improves the performance by 0.4% in DSC on the CAMUS dataset compared to independently using the \mathcal{L}_{uns} in No. 3.

D.2 Effect of Candidate Operation Set

Method	DSC \uparrow	IoU \uparrow	95HD \downarrow
Include pooling and no connection	0.924 _(0.005)	0.923 _(0.004)	2.961 _(0.238)
Exclude pooling and no connection	0.933_(0.002)	0.931_(0.002)	2.480_(0.161)
Gain	\uparrow 0.009	\uparrow 0.008	\downarrow 0.481

Table 8: Ablation study on the set of decoder candidate operations on the HMC-QU dataset.

Table 8 presents an ablation study that investigates the effect of including or excluding pooling and no connection operations from the set of candidate operations for the decoder component, evaluated on the HMC-QU dataset. The differences between the two scenarios are quantified in the final row, demonstrating that excluding pooling and no connection operations from the decoder cells leads to superior performance across all three evaluation metrics.

These empirical findings suggest that, for the given task and dataset, a simpler decoder architecture without pooling and no connection operations is more effective in achieving

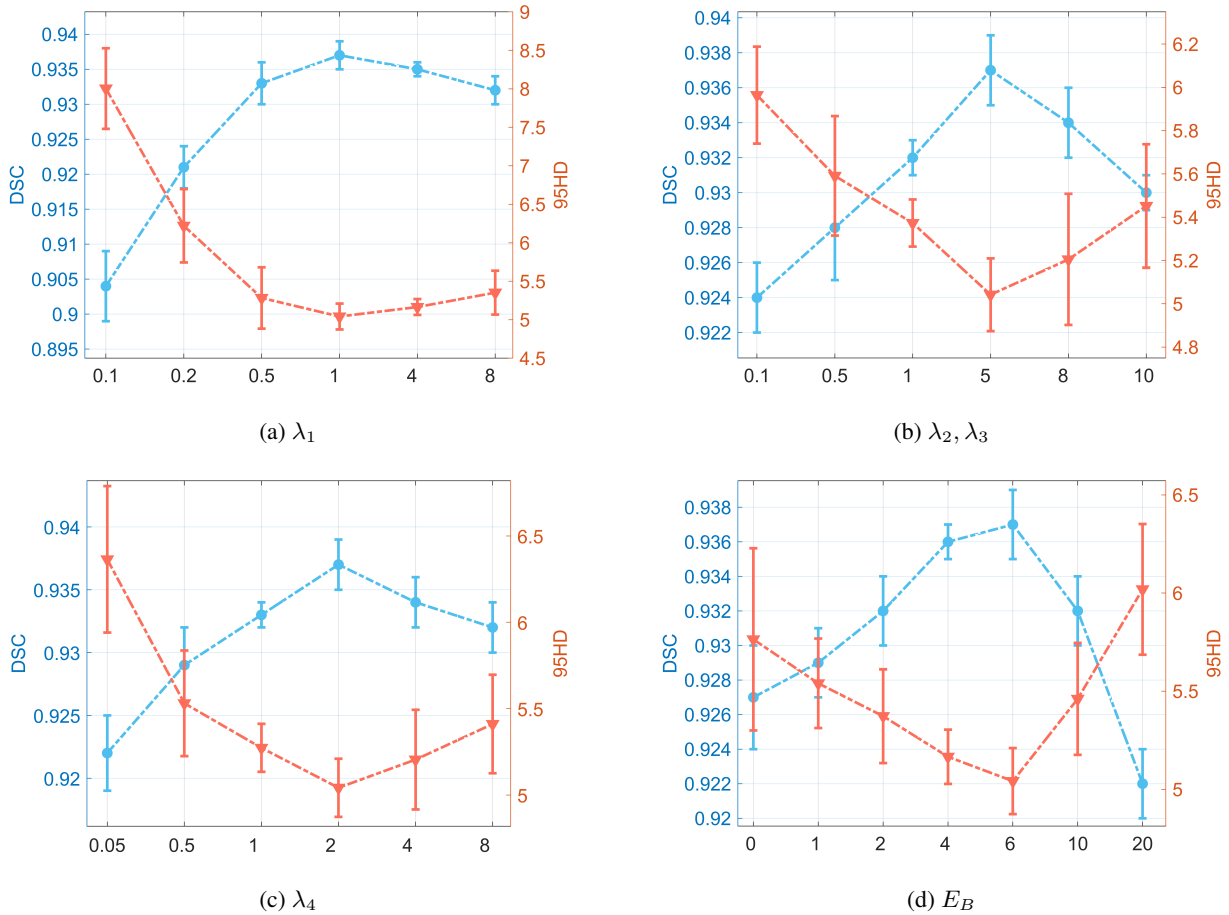


Figure 16: Ablation experiments on different hyper-parameters on the CAMUS dataset. (a) Supervised loss coefficient λ_1 . (b) Unsupervised loss coefficient λ_2 and network independence loss coefficient λ_3 . (c) Contrastive loss coefficient λ_4 . (d) Beta epochs E_B , which denotes the level of emphasis placed on algorithmic independence.

superior segmentation performance. The inclusion of these operations appears to be detrimental, potentially introducing noise or feature degradation that outweighs any potential benefits.

D.3 Impact of Contrastive Loss at Different Feature Resolutions

Method	DSC \uparrow	IoU \uparrow	95HD \downarrow
None	0.924 _(0.002)	0.922 _(0.001)	2.852 _(0.102)
$r \in \{4, 8\}$	0.929 _(0.001)	0.928 _(0.001)	2.603 _(0.115)
$r \in \{4, 8, 16\}$	0.933 _(0.002)	0.931 _(0.002)	2.480 _(0.161)
$r \in \{4, 8, 16, 32\}$	0.927 _(0.002)	0.926 _(0.001)	2.719 _(0.148)

Table 9: Ablation Studies on different stages calculated in contrastive loss \mathcal{L}_{con} on the HMC-QU dataset.

We further investigate whether incorporating the contrastive loss \mathcal{L}_{con} at different feature resolutions can improve the model performance on the HMC-QU dataset. We gradually combine intermediate features from resolutions

$r \in \{4, 8, 16, 32\}$. As shown in Table 9, the performance is promoted by gradually incorporating resolutions from $r = 4$ to $r = 16$. Nevertheless, the performance decreases when leveraging the $r = 32$. This is mainly because feature maps at $r = 32$ contain high-level semantic information but lack detailed information necessary for contrastive analysis, and then the loss computed at this resolution does not contribute to the improvement.

E More Hyper-parameter Studies

E.1 Sensitivity to Loss Coefficients

The sensitivity to hyper-parameter settings of loss coefficients is also discussed, under a 50% annotation ratio on the CAMUS dataset. As shown in Fig. 16(a), the fluctuations in DSC caused by varying λ_1 indicate that the supervised loss plays a dominant role. From Fig. 16(b), we observe that assigning a low weight to the initial value of λ_2 weakens the role of the co-training. While setting to a high value, it causes HCS-TNAS to deviate from the main segmentation task. This principle is also applicable to the contrastive loss coefficient λ_3 . As observed in Fig. 16(c) and (d), the degree

of emphasis on network independence has an obvious influence. When $\lambda_4 = 2$ and $E_B = 6$, we obtain the highest DSC, whereas assigning a small weight to the independence loss fails to utilize the advantage of co-training, and a small number of iterations also lead to insufficient network independence estimation. On the other hand, an excessive focus on independence causes the NAS backbone to deviate from the optimum.

E.2 Sensitivity to Network Layers

Method	HMC-QU	CAMUS	CETUS
4	0.920 _(0.002)	0.866 _(0.002)	0.969 _(0.002)
6	0.928 _(0.001)	0.879 _(0.003)	0.978 _(0.002)
8	0.931 _(0.002)	0.884 _(0.003)	0.978 _(0.001)

Table 10: Hyper-parameter study on the impact of different numbers of network layers L on three datasets. The evaluation metric is IoU.

To evaluate the effect of the number of network layers L , the network is initialized with 4, 6, and 8 layers, respectively, while maintaining the other parameters constant to facilitate a fair comparison. The quantitative results obtained across the HMC-QU, CETUS, and CAMUS datasets are presented in Table 10. It can be observed that the proposed model employing 8 layers achieves superior performance in comparison to using 4 and 6 layers. Based on this finding, L in our model is initialized to 8.

F Future Work

Our future work is to further enhance the zero-shot generalization capability (zero-shot learning) of our model. Specifically, while our current approach involves training on ultrasound image datasets, we aim to investigate the model’s transferability and robustness by evaluating its performance on other medical imaging modalities, such as magnetic resonance imaging (MRI) or computed tomography (CT) scans. In other words, we hope that the model can effectively perform tasks without having encountered specific examples of those tasks or domains during training.

This cross-modality research will provide insights into the model’s ability to generalize and adapt to diverse imaging data, which is crucial for practical clinical applications. By enhancing zero-shot generalization capability across modalities, we strive to develop a more versatile and robust solution for medical image analysis workflows, ultimately contributing to improved patient care.